Role of Cr in Mn-rich precipitates for Al–Mn–Cr–Zr-based alloys tailored for additive manufacturing

Downloaded from: https://research.chalmers.se, 2025-12-08 23:27 UTC

Citation for the original published paper (version of record):
Mehta, B., Frisk, K., Nyborg, L. (2024). Role of Cr in Mn-rich precipitates for Al–Mn–Cr–Zr-based alloys tailored for additive
manufacturing. Calphad: Computer Coupling of Phase Diagrams and Thermochemistry, 84.
http://dx.doi.org/10.1016/j.calphad.2024.102667

N.B. When citing this work, cite the original published paper.

research.chalmers.se offers the possibility of retrieving research publications produced at Chalmers University of Technology. It covers all kind of research output: articles, dissertations, conference papers, reports etc. since 2004. research.chalmers.se is administrated and maintained by Chalmers Library

(article starts on next page)

CALPHAD: Computer Coupling of Phase Diagrams and Thermochemistry 84 (2024) 102667

Contents lists available at ScienceDirect

Calphad

journal homepage: www.elsevier.com/locate/calphad

Role of Cr in Mn-rich precipitates for Al–Mn–Cr–Zr-based alloys tailored for additive manufacturing

B. Mehta [a,b,*], K. Frisk [a], L. Nyborg [a]

[a] Department of Industrial and Materials Science, Chalmers University of Technology, Rännvägen 2A, Göteborg, 41296, Sweden
[b] Department of Materials Science and Engineering, KTH Royal Institute of Technology, Brinellvägen 23, Stockholm, 10044, Sweden

ARTICLE INFO

Handling Editor: Prof. Z.K. Liu

Keywords:
Additive manufacturing
Powder bed fusion-laser beam
Aluminium alloys
Precipitation kinetics

ABSTRACT

Novel alloy concepts enabled via additive manufacturing processes have opened up the possibility of tailoring properties beyond the scope of conventional casting and powder metallurgy processes. The authors have previously presented a novel Al–Mn–Cr–Zr-based alloy system containing three times the equilibrium amounts of Mn and Zr. The alloys were produced via a powder bed fusion-laser beam (PBF-LB) process taking advantage of rapid cooling and solidification characteristics of the process. This supersaturation can then be leveraged to provide high precipitation hardening via direct ageing heat treatments. The hardening is enabled with Zr-rich and Mn-rich precipitates. Literature study confirms that Mn-rich precipitates have a notable solubility of Cr, for example, the Al12Mn precipitate. This study aims to clarify the effect of Cr solubility in the thermodynamics and kinetics simulation and compare the precipitation simulations with samples subject to >1000 h isothermal heat treatment, thus creating an equilibrium-like state. The results show that Cr addition to the precipitates stabilizes the Al12Mn precipitate while slowing the precipitation kinetics thus producing a favourable hardening response. Such observations could be insightful while designing such alloys and optimising heat treatments of the current or even a future alloy system.

1. Introduction

Additive manufacturing (AM) of metals is a relatively new processing route for producing components at a large scale [1]. It has been previously used for prototyping and creating complex components otherwise not manufacturable with conventional techniques [2]. With advances in the understanding of the process, several industries have been able to create novel products with this manufacturing process which are not possible with conventional methods [3]. The most commonly used AM process is powder bed fusion-laser beam (PBF-LB) wherein a focused laser beam selectively melts a thin layer of metal powder (20–80 μm in thickness) to create components layer by layer [4]. Apart from the product design freedom that the method provides, it is well known that higher cooling rates (10^3–10^5 K/s) [5] are achieved. These cooling rates translate into an increased alloy design freedom, which has been shown successfully for several Al-alloys [6–9]. Researchers have shown that such tailored alloys perform extremely well for the application they are designed for. Plotkowski et al. [9] showed that Al–Ce–Mn alloys showed promising high-temperature strength and Schmidtke et al. [8] showed a novel Al–Mg-Sc-Zr-based alloy which is suitable for high-strength applications.

Most Al-alloys derive a major part of their strength via precipitation hardening [10,11]. Precipitation hardening seldom comes from primary precipitates formed upon solidification but rather relies on secondary precipitation that takes place on heat treatment [12]. When it comes to alloys tailored for the PBF-LB process, higher supersaturation in the Al-matrix can be leveraged to drive a higher amount of homogenous precipitation via secondary precipitation reactions. We have previously shown for Al–Mn–Cr–Zr-based alloy systems that direct ageing results in the precipitation of Mn-rich and Zr-rich precipitates causing an increase in hardness by 40 HV for one of the alloys containing Cr [13]. The precipitation hardening was lower (25 HV) for the alloys free from Cr. This difference was hypothesised to largely originate from the effect of Cr on Mn-rich precipitates as some Cr pickup was observed for these precipitates during chemical microanalysis [13]. Such a Cr effect was postulated to further affect the precipitation kinetics of Zr-rich precipitates which were observed to co-precipitate with Mn-rich precipitates. Another partial explanation could be due to small differences in chemical compositions between the alloys, though the difference was quite low. Initially, we could not reproduce the Cr effect on Mn-rich

* Corresponding author. Department of Industrial and Materials Science, Chalmers University of Technology, Rännvägen 2A, Göteborg, 41296, Sweden.
E-mail addresses: bharat.mehta@chalmers.se, bmehta@kth.se (B. Mehta).

https://doi.org/10.1016/j.calphad.2024.102667
Received 3 September 2023; Received in revised form 25 January 2024; Accepted 5 February 2024
Available online 19 February 2024
0364-5916/© 2024 The Authors. Published by Elsevier Ltd. This is an open access article under the CC BY license (http://creativecommons.org/licenses/by/4.0/).

precipitates utilising CALculations of PHAse Diagrams (CALPHAD) tools as the thermodynamic parameters in the databases available to us when the alloy system was developed, did not contain parameters for Cr connected to the Mn-rich precipitates.

Therefore, this study delves deeper into the two pieces of missing information and explains them via CALPHAD methods coupled with advanced characterisation tools. Thermodynamic parameters related to the solubility of Cr in Mn-rich precipitates were modified based on the experimental data reported in the literature and the characterisation of samples produced from one of the alloys of the Al–Mn–Cr–Zr based system which was heat treated at 350 °C for >1000 h in this work. The input showed a stabilisation of Al12Mn precipitate as expected. Finally, precipitation calculations were conducted utilising the precipitation module (TC-PRISMA) in Thermo-Calc software [14], focusing on Mn-rich precipitates to illustrate the change in precipitation kinetics.

2. Materials, experimental and simulation setup

The material used is called alloy C (similar to our previous studies [7,13]). The source material is spherical nitrogen (N_2) gas-atomised powder provided by Höganäs AB, Sweden with a standard powder size distribution of 20–53 μm. The chemistry is summarised in Table 1.

Solid samples were manufactured using an EOS M100 PBF-LB machine equipped with a Yb-fiber laser. The samples were produced as a 10 mm × 10 mm x 16 mm (l x w x h) cube and produced with laser power 170 W, laser speed 1500 mm/s, 0.1 mm hatch distance and 0.03 mm layer thickness [13]. During manufacturing, samples had scan rotation of 67° between each layer. After manufacturing, the samples were heat treated in a resistance furnace with a secondary thermocouple close to the sample surface for temperature control within ± 2K. The samples were first peak aged at 350 °C for 24 h as established in previous studies [13]. After peak ageing, the samples were heat treated at 350 °C for 1054 h, as initially studied in Ref. [15]. Thus, the total heat treatment on the sample from the as-printed condition to the overaged condition constituted 1078 h of heat treatment at 350 °C from as-printed condition, creating a nominal equilibrium-like state. Scanning electron microscopy (SEM) samples were produced by grinding and polishing the samples as per the standard preparation procedure for such alloys on a Struers TegraPol 31 machine. The final step of OP-S silica suspension was used for preparing samples for electron microscopy. A Zeiss Gemini 450 electron microscope equipped with ULTIM MAX Energy Dispersive X-ray Spectroscopy (EDS) detector from Oxford Instruments enabled precipitate analysis at low voltages (<5 kV) thus making it possible to study nanoprecipitates. Electron Backscatter Diffraction (EBSD) measurements were conducted on freshly polished samples at 10 kV, 10 nA settings using a Symmetry CMOS EBSD detector from Oxford Instruments. The samples were scanned with a step size of 0.04 μm. The EBSD data was produced using Aztec v6 from Oxford Instruments and was later processed using Aztec Crystal software. The raw data was processed using Aztec Crystal and auto cleanup was conducted for normalizing the data. The simulations were performed with the Thermo-Calc 2022a software package [16] and for the precipitation module (TC-PRISMA) [14]. The database comparisons were done using the COST507 database [17], a quinary Al–Mn–Cr–Zr–Fe subset of Thermo-Calc Software AB's TCAL8 database, and our amended database.

Table 1
Composition of alloy C obtained via inductively coupled plasma-atomic emission spectroscopy (ICP-AES) reported before [13]. Compositions provided as atomic% (at%) and weight% (wt%).

Element	Composition (at%/wt%)					
	Al	Mn	Cr	Zr	Fe	Si
	Rem.	2.53/5.0	0.43/0.8	0.18/0.6	0.08/0.16	0.17/0.17

3. Results and discussion

3.1. Current state-of-the-art

For this alloy system (Al–Mn–Cr–Zr based), the COST507 database [17] (Al–Mn–Cr–Zr–Fe–Si) and a quinary database provided by Thermo-Calc Software (Al–Mn–Cr–Zr–Fe) have been considered as state-of-the-art databases. Some important ternary systems in this quinary frame of elements such as Al–Fe–Mn are already well documented due to their applicability in commercial aluminium alloys [11,13] and one of the available thermodynamic databases has a good description of effects such as Fe addition in Mn-rich phases. The stabilising effect of Fe on the Al6Mn phase can be shown with ternary Al–Fe–Mn diagrams [13]. However, the role of Cr in Mn-rich phases is not available. Grushko et al. [18] presented experimental data on the constitution of the Al-rich part of the Al–Mn–Cr ternary system and Cui and Jung [19] have presented a thermodynamic assessment of the Al–Mn–Cr ternary system wherein Cr effects in Mn-rich phases namely Al12Mn and Al6Mn are well documented. The available commercial databases lack this description of the ternary Al–Mn–Cr system, which could describe the solubility of Cr into different Mn-rich phases or vice versa. Experimental work on Al–Mn–Cr systems [20,21] has shown that there exists a solubility of Cr in at least one of the Mn-rich phases (tentatively Al12Mn). The results are summarised in Table 2. This means that if the thermodynamic databases are adjusted for Cr solubility in such phases, it could be more representative of the precipitation kinetics of the alloy system studied by us (Al–Mn–Cr–Zr-based). Mondolfo [20] also postulated that Mn is completely soluble in Al13Cr2 (labelled as Al45V7 in the Al–Mn–Cr–Zr–Fe database) phase. However, this study is focusing only on the effect of Cr solubility in Mn-rich phases.

As summarised in Fig. 1 and Table 3, the one-axis equilibrium curves suggest that both databases provide a similar description in terms of the formation of different phases. The formation of the AlMnSi_alpha phase is not possible in the Al–Mn–Cr–Zr–Fe database due to the absence of Si in the description. The small difference that exists between the two databases is the amount of Al12Mn phase formed. For the Al–Mn–Cr–Zr–Fe database, this phase starts forming at a similar temperature (~410 °C) as with the COST507 database (~400 °C). However, when comparing the amounts predicted to be formed at 350 °C, which is the temperature of long-term heat treatment, the amounts are quite different, namely 0.143 and 0.06 mol fractions, respectively. This suggests that Al12Mn is slightly more stable in the Al–Mn–Cr–Zr–Fe database description than in the COST507 database description at 350 °C.

3.2. Microstructure characterisation of equilibrium-like state

Electron microscopy was conducted to characterize the microstructure of an overaged sample of alloy C, heat treated at 350 °C 1054 h after peak ageing (350 °C 24 h). This condition is assumed to represent an equilibrium-like condition. Fig. 2 shows the microstructure before and after such long heat treatment. As seen in Fig. 2a)-b), the microstructure has in as-printed condition elongated Al-grains from the layer-by-layer PBF-LB processing, which is common for such materials [25]. The amount and size of precipitates are very low (<1 area% [7,13]) which suggests close to full supersaturation of solutes. After the long-term heat treatment, as shown in Fig. 2c) onwards, a high number of precipitates are observed (about 18% area [15]), with preferential growth having

Table 2
Experimental chemical composition found in various Mn-rich phases in rapid solidification literature for Al–Mn–Cr ternary systems.

Phase	Cr (wt%)	Fe (wt%)	Mn (wt%)	Reference
G-Al12(Mn,Cr)	2–4	–	10–12	[20,22]
Al6Mn	–	0–13	14–27	[20,23,24]
Al45V7 (Al13Cr2)	0–27	–	0–27	[20]

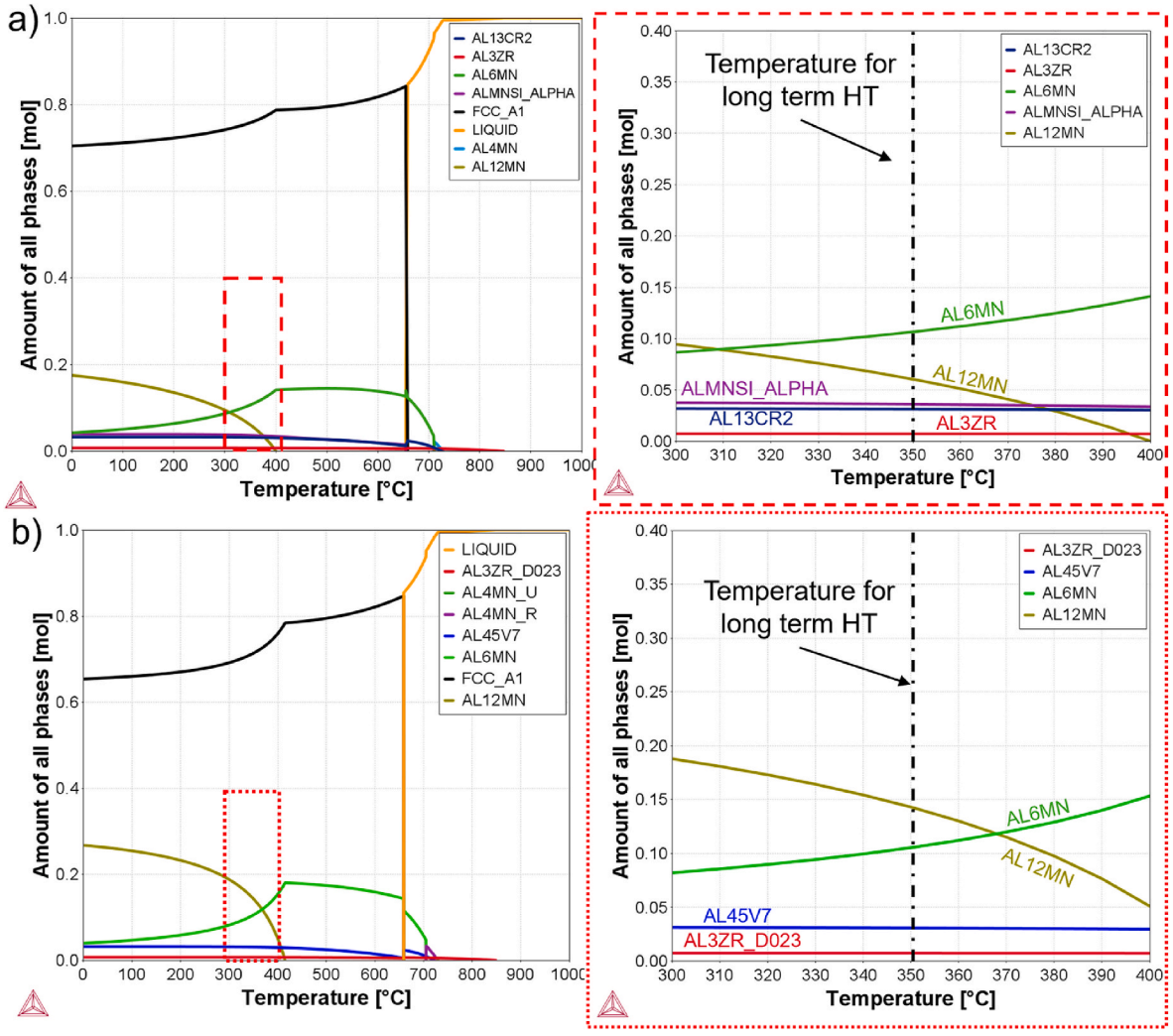

Fig. 1. *One-axis step equilibrium calculations prepared using a) COST507 database [13,17] and b) Al–Mn–Cr–Zr–Fe database. Calculations conducted on Alloy C composition from Table 1. The insets for both images show the distribution of different phases between 300-400 °C, at equilibrium. Long-term heat treatment (HT) tests were conducted at 350 °C (shown with a black dot-dash line in inset images).*

Table 3
Mole fraction of various phases formed at equilibrium at 350 °C (623 K) shown in Fig. 1.

Phase	Mole fraction (COST507)	Mole fraction (Al–Mn–Cr–Zr–Fe database)
FCC_A1 (Aluminium)	0.758	0.713
Al6Mn	0.107	0.106
Al12Mn	0.061	0.143
Al3Zr/Al3Zr_D023	0.007	0.007
AlMnSi_Alpha	0.036	–
Al13Cr2/Al45V7	0.031	0.031

occurred at grain boundaries. Most of these precipitates are enriched in Mn. Fig. 2d) shows the microstructure associated with the interior of melt pools and large micrometre-sized precipitates can be seen in the inset image. The precipitates can be differentiated as having a dark or bright contrast. The darker contrast precipitates are mostly present at grain boundaries (marked with red) whereas the bright contrast precipitates could be either present at grain boundaries or inside the grains. The grain boundary precipitates are elongated with length >10 μm but have restricted width <2 μm. Those inside the grains are much smaller than grain boundary precipitates; they are also elongated with length ~1–2 μm and width <0.5 μm. Micro-chemical characterisation using EDS point scans was conducted on both types (dark and bright contrast) of Mn-rich precipitates at grain boundaries utilising low voltage mode (5 kV) to obtain better spatial resolutions. The focus was kept mostly on grain boundary precipitates to avoid drift issues or limited spatial resolutions. As summarised in Fig. 3, it was observed that the darker contrast precipitates contain about 8 at% Mn together with Fe (0.31 at %) and Cr (0.67 at%). This suggests that these precipitates had stoichiometry close to Al12Mn (7.69 at% Mn) and possibly containing Cr and Fe. Secondly, the bright contrast precipitates contained about 14 at % Mn together with Fe (1.19 at%) and Cr (0.25 at%). This suggests that these precipitates had stoichiometry closer to Al6Mn (14.3 at% Mn) and were rich in Fe. Based on initial analysis, EBSD studies were also conducted to confirm the phases based on Kikuchi patterns. Possible candidate phases of interest were taken from the inorganic crystal structure database [26]. Several phases namely G-Al12(Mn, Cr) (called Al12Mn before) [22], Al6(Mn, Fe) (called Al6Mn before) [23], AlMnSi_alpha [27] and Al45Cr7 (called Al45V7 before) [28] were tested for the overaged sample of alloy C. As seen in Fig. 4, the precipitates appear to belong mostly to either Al12Mn or Al6Mn precipitate families with reasonable mean angular deviation (MAD) values. There were a few locations where smaller AlMnSi_alpha or Al45Cr7 was observed but most of the precipitates close to grain boundaries were characterized either as Al12Mn or Al6Mn. However, it needs to be added that

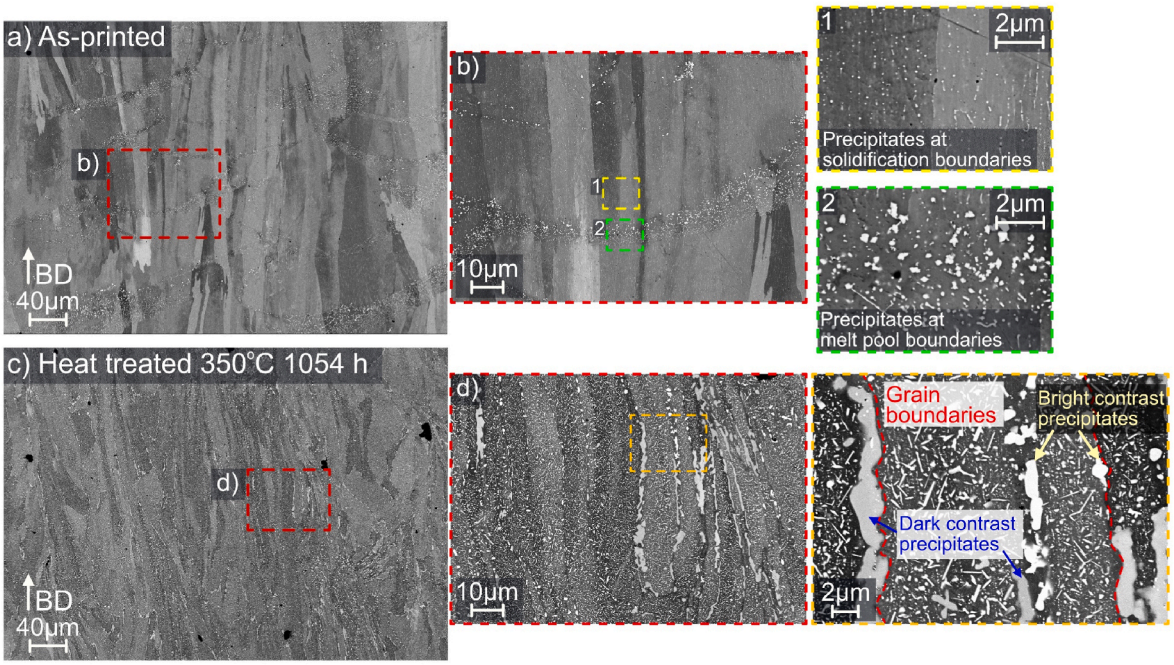

Fig. 2. Electron microscopy a) Alloy C as-printed condition and inset b) showing few nanoscale precipitates formed at different areas as inset 1,2 respectively c) Alloy C heat treated at 350 °C for 1054 h after peak hardening. Inset d) shows larger precipitates where another higher magnification image shows different precipitates and grain boundaries.

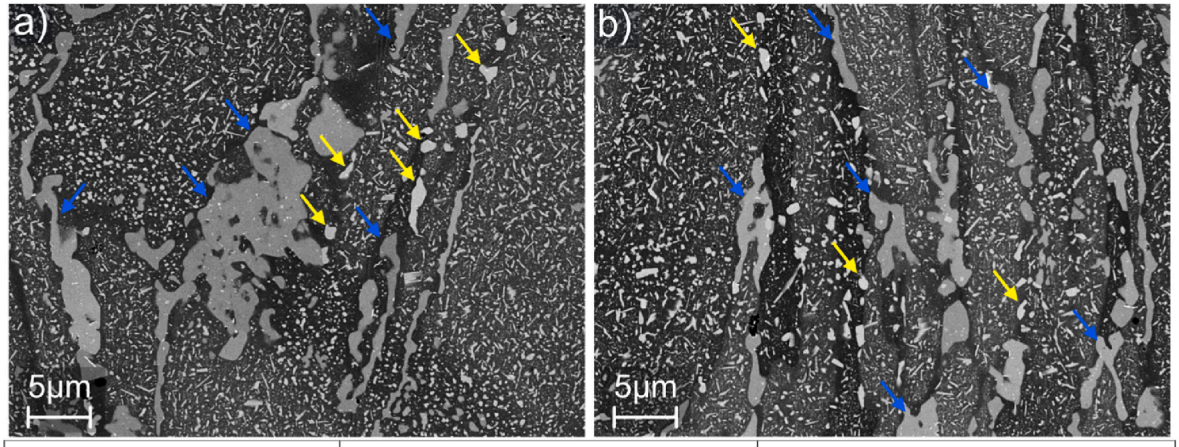

	Blue ppt	Yellow ppt
Concentration (at% / wt%)		
Si	0.02/ 0.02	0.01/ 0.01
Cr	0.67/ 1.18	0.25/ 0.41
Mn	8.01/ 14.89	14.03/ 24.53
Fe	0.31/ 0.58	1.19/ 2.12
Zr	0.07/ 0.20	0.06/ 0.16
Al	Rem.	Rem.

Fig. 3. a)-b) Two areas where EDS point scans were conducted. Precipitates marked in blue and yellow and their respective chemical composition shown.

AlMnSi_alpha and Al12Mn precipitate both possess a cubic lattice with parameters which could be hard to differentiate using the EBSD technique. We observed that the stoichiometry of the precipitates in Fig. 3 failed to pick up any Si, thus suggesting that there is a higher likelihood of the darker contrast phase representing the cubic Al12Mn phase.

3.3. Modification of thermodynamic parameters

Thermodynamic parameters from Cui and Jung [19] were used as a starting point and later adjusted to match the experimental results. As per Cui and Jung [19], the parameters for Al6Mn and Al12Mn are

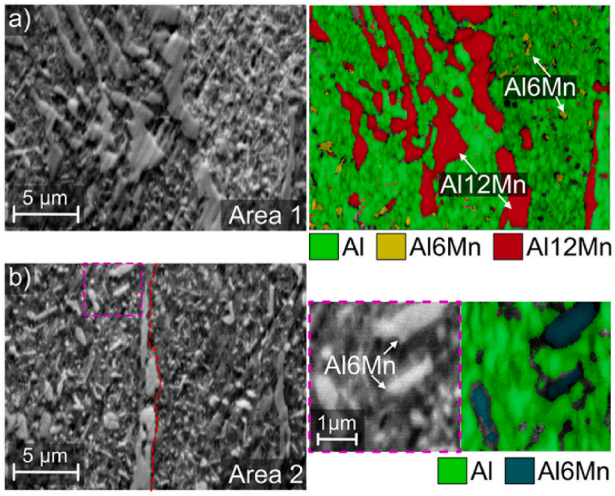

Phase	Phase %	Avg. MAD
Al	70.3	0.74
Al12Mn	21.8	0.61
Al6Mn	1.6	1.07
Zero solution	6.3	

Phase	Phase %	Avg. MAD
Al	74.2	0.7
Al12Mn	0.1	0.89
Al6Mn	10.3	0.59
Zero solution	15.4	

Fig. 4. High-resolution EBSD phase maps for two areas in overaged alloy C shown. a) Area 1 illustrates an area where mostly Al12Mn precipitates (red), Al (green) and possibly some Al6Mn (yellow) are seen b) Area 2 illustrates an area where grain boundary (orange) is shown. An inset (red) was scanned at higher magnification where Al6Mn precipitates (dark green) and Al (green) was shown.

provided as follows.

3.3.1. Initial thermodynamic parameters

Parameters for: Al_6Mn ; $(Al)_6(Mn,Cr)$.

${}^{o}G_{Al:Mn} = -109091 + 35.22\,T + 6\,{}^{o}G_{Al}^{fcc} + {}^{o}G_{Mn}^{cbcc}$ [29].

${}^{o}G_{Al:Cr} = -83680.0 + 6\,{}^{o}G_{Al}^{fcc} + {}^{o}G_{Cr}^{bcc}$.

${}^{o}L_{Al:Mn,Cr} = -60249.6 + 41.84T$.

Parameters for: $G_{Al_{12}Mn}$; $(Al)_{12}(Mn,Cr)$.

${}^{o}G_{Al:Mn} = -110389.5 + 36.8\,T + 12\,{}^{o}G_{Al}^{fcc} + {}^{o}G_{Mn}^{cbcc}$ [29].

${}^{o}G_{Al:Cr} = -97336.58 + 83.68T + 12\,{}^{o}G_{Al}^{fcc} + {}^{o}G_{Cr}^{bcc}$.

${}^{o}L_{Al:Mn,Cr} = -178137.98 + 37.66T$.

${}^{1}L_{Al:Mn,Cr} = 116993.01 - 52.30T$.

At the same time, Cui & Jung [19] and Grushko et al. [18] argued that Cr has solubility in both Al6Mn and Al12Mn. However, from our experiments, we found a low Cr solubility in Al6Mn at 350 °C (see Fig. 3) which agrees more with literature evidence on experimental alloys (see Table 2). Thus, further modification to the thermodynamic parameters of Al12Mn and Al6Mn was conducted to have modified parameters agree with our experimental observations. Table 4 shows the experimental and calculated composition of the Al6Mn and Al12Mn phases for Alloy C. It could however be possible that some Cr solubility exists at higher temperatures for Al6Mn (>500 °C) [18,19]. After several iterations, the final parameters were as follows. The ${}^{1}L_{Al:Mn,Cr}$ parameter from the initial description was removed (see Table 5).

3.3.2. Final thermodynamic parameters

Parameters for: Al_6Mn ; $(Al)_6(Mn,Cr)$.

Table 4
Comparison of experimental and calculated chemistries of Al12Mn and Al6Mn precipitates. Calculated concentrations derived from modified thermodynamic parameters using quinary Al–Mn–Cr–Zr–Fe database. Contents are written as at %/wt% for each element respectively.

Condition	Phase	Mn	Cr	Fe	Zr
Experimental 350 °C 1054 h [Fig. 3]	Al12Mn	8.01/ 14.89	0.67/ 1.18	0.31/ 0.58	0.07/ 0.2
	Al6Mn	14.03/ 24.53	0.25/ 0.41	1.19/ 2.12	0.06/ 0.16
Calculated at 350 °C equilibrium [modified parameters]	Al12Mn	6.51/ 12.30	1.18/ 2.11	–	–
	Al6Mn	9.93/ 17.61	0.26/ 0.44	4.08/ 7.36	–

Table 5
Mole fraction of various phases predicted for equilibrium at 350 °C (623 K) shown in.

Amount of phase at 350 °C	
Phase	Mole fraction
Al	0.614
Al12Mn	0.359
Al6Mn	0.020
Al3Zr_D023	0.007

${}^{o}G_{Al:Mn} = -109091 + 35.22\,T + 6\,{}^{o}G_{Al}^{fcc} + {}^{o}G_{Mn}^{cbcc}$ [29]

${}^{o}G_{Al:Cr} = -73000 + 6\,{}^{o}G_{Al}^{fcc} + {}^{o}G_{Cr}^{bcc}$ [This work].

${}^{o}L_{Al:Mn,Cr} = -60249.6 + 41.84T$ [19]

Parameters for: $G_{Al_{12}Mn}$; $(Al)_{12}(Mn,Cr)$.

${}^{o}G_{Al:Mn} = -110389.5 + 36.8\,T + 12\,{}^{o}G_{Al}^{fcc} + {}^{o}G_{Mn}^{cbcc}$ [29]

${}^{o}G_{Al:Cr} = -97336.58 + 83.68T + 12\,{}^{o}G_{Al}^{fcc} + {}^{o}G_{Cr}^{bcc}$ [19]

${}^{o}L_{Al:Mn,Cr} = -95000 + 18.83T$ [This work].

The resulting compositions of the Al6Mn and Al12Mn phases are shown in Fig. 3 and Table 4. The one-axis equilibrium using the modified parameters is drawn in Fig. 5. It shows that an even higher amount of Al12Mn is stabilised at 350 °C (0.36 mol fraction as compared to 0.06/0.14 mol fraction in Fig. 1), which is a consequence of the Cr solubility as is also evident from the literature [20,21]. The concentration of Cr in Al12Mn and Al6Mn precipitates at 350 °C were 1.2 at% and 0.26 at% respectively. As per Table 4, about 0.67 at% and 0.25 at% Cr were seen in the precipitates which is following the trend of the experimental observations, though the experimental concentration in Al12Mn was half. Fe solubility is predicted to be 0 at% and 4.08 at% in Al12Mn and Al6Mn respectively. The results from EDS showed 0.31 at% and 1.19 at %, which shows a similar trend, although the values are different. We chose not to modify the parameters for the Fe solubility further as the study focuses only on the Cr effect on Mn-rich precipitates. Another reason for the difference in stoichiometries of the precipitates observed experimentally as compared to Table 2 could be the limitations of the microscope. On the one hand, we chose 5 kV as accelerating voltage to obtain good spatial resolution. However, this meant that Lα lines were the ones analysed. For Cr, Mn and Fe, these lines are close to one another at 654 eV, 722 eV and 792 eV respectively [30], thus making it harder to discriminate between these elements with the help of EDS. On the other hand, Kα lines for these elements are at 5415 eV, 5900 eV and 6405 eV,

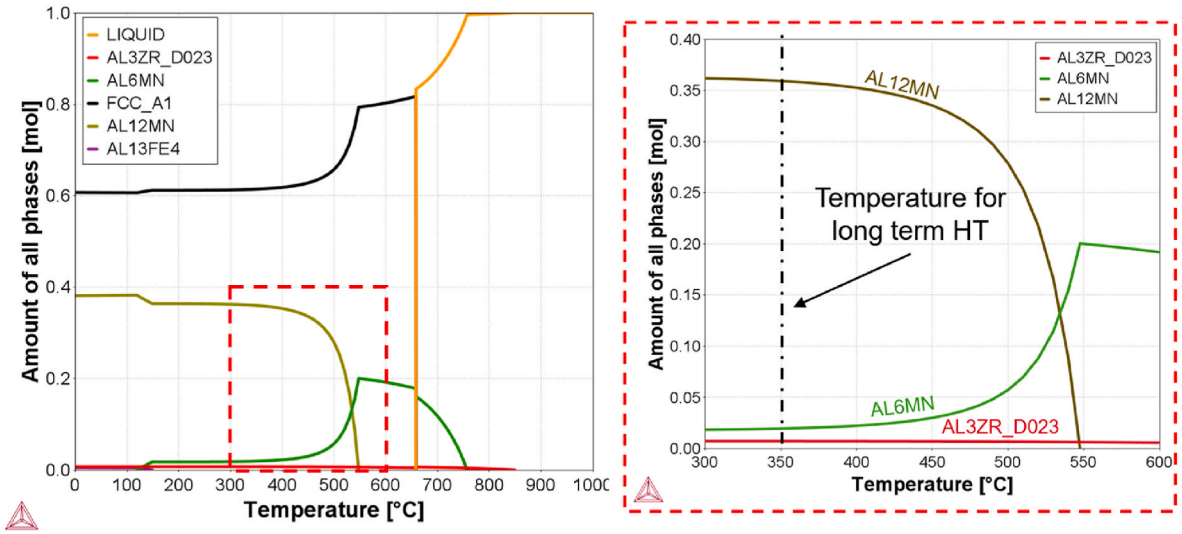

Fig. 5. One-axis step equilibrium prepared using final modified parameters for Al12Mn and Al6Mn.

which would make it easier to discriminate between the elements. An accelerating voltage of >15 kV would be needed, which would make the spatial resolution >2 μm in an SEM. Some EDS point scans at similar locations were tried with both 5 kV and 15 kV and it was seen that for a similar location, Mn peaks concentration of 8 at% and 6.5 at% were detected respectively. Since the width of the precipitate is smaller than the spatial resolution, Mn from the matrix is picked up, which makes the analysis inaccurate. The best solution would be to investigate the chemistry using transmission electron microscopy combined with high-resolution EDS. Additionally, as per [18,19], the Al12Mn phase was stable only at temperatures <600 °C. As seen in Fig. 6, the calculated phase diagram shows that Al12Mn disappears at 600 °C but is stable at 500 °C and 550 °C. This is in line with observations of Cui & Jung [19], Grushko et al. [18] and Ohnishi et al. [31]. This fact was considered when adjusting the parameters. The two-phase region with higher Cr as shown by Cui & Jung [19] contains Al + Al12Mn. In our phase diagram, it seems to be Al + Al6Mn which is different. It indicates that future work may be needed at higher temperatures and with assessment of Cr-phase (Al45V7) for a better comparison.

3.4. Precipitation kinetics of the resulting database

Finally, precipitation simulations were performed using the TC-PRISMA module in Thermo-Calc software as shown in Fig. 7. The

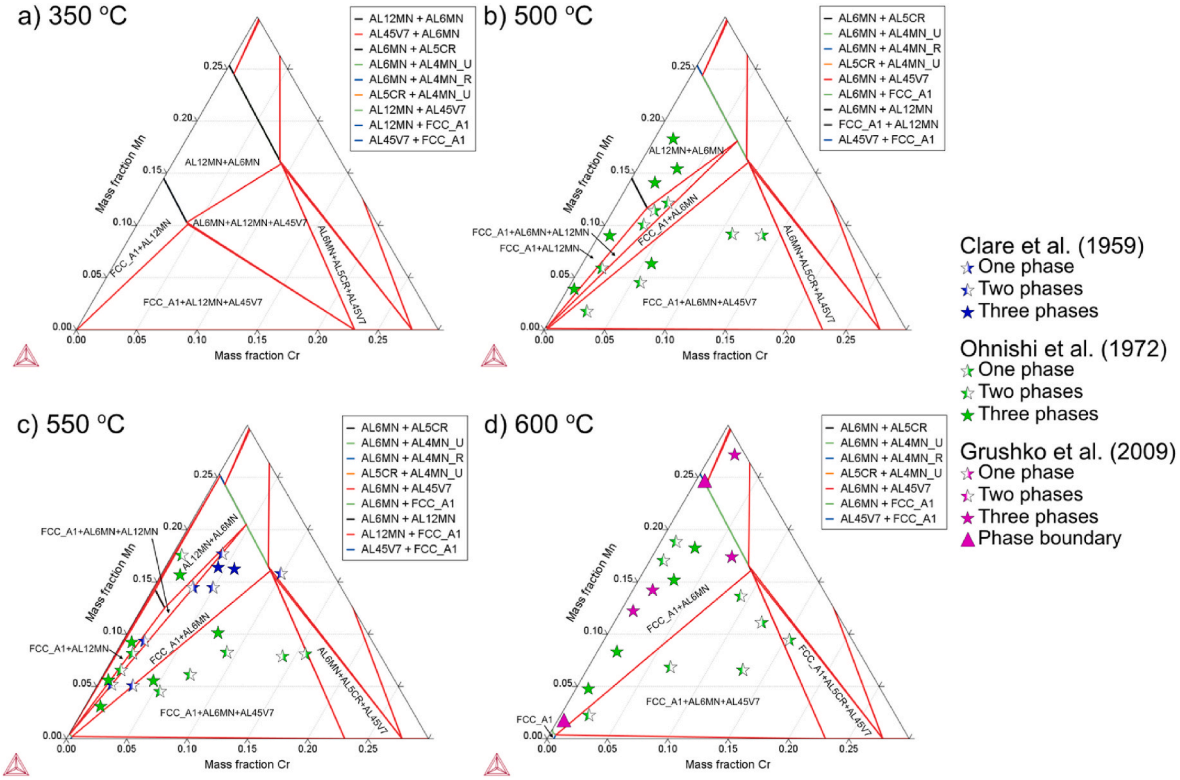

Fig. 6. *a)-d) Ternary diagrams for Al–Mn–Cr with modified parameters at 350 °C, 500 °C, 550 °C and 600 °C respectively. Experimental data from other works* [18,19,31,32] has been mentioned with respective colour codes.

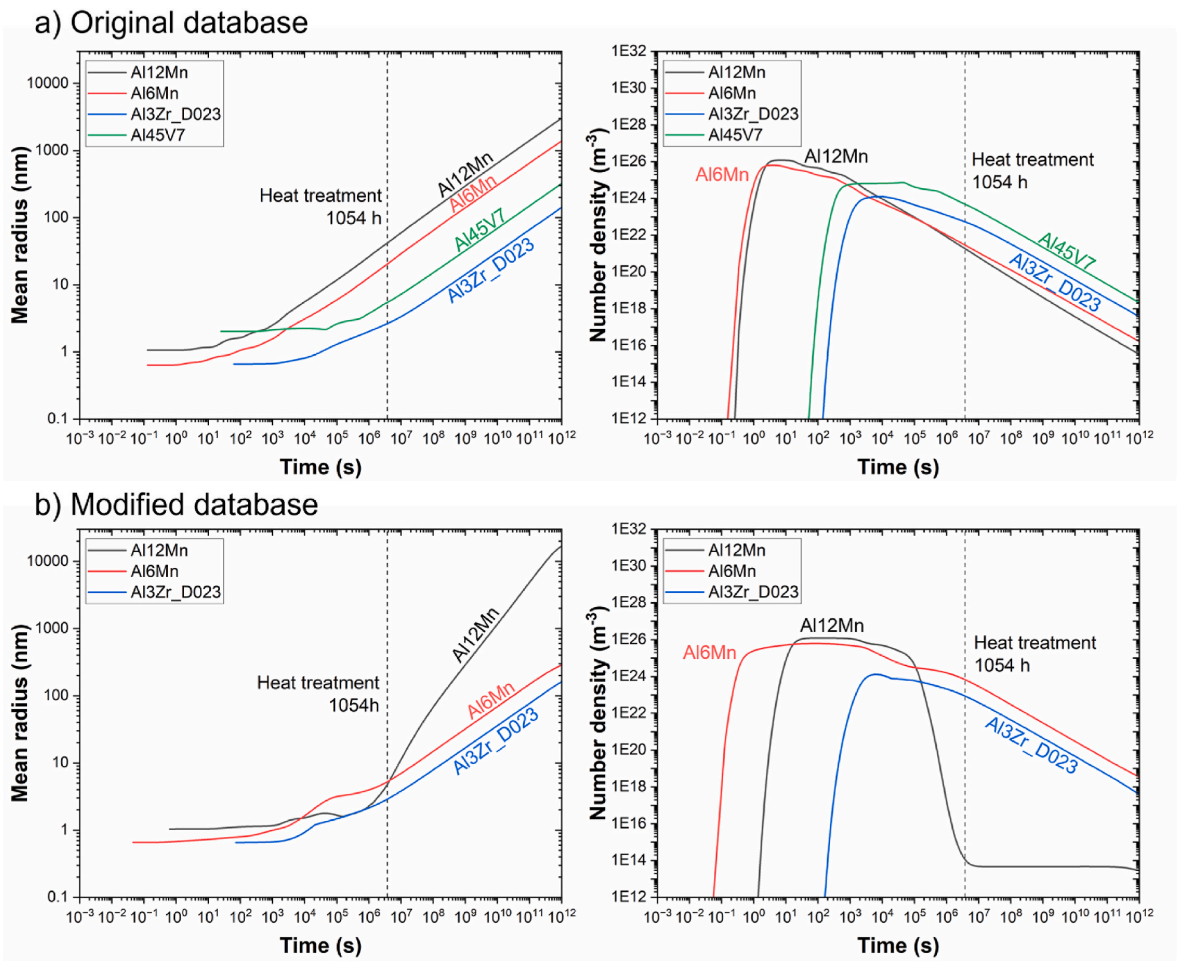

Fig. 7. TC-PRISMA calculations comparing a) original Al–Mn–Cr–Zr–Fe database and b) modified database. Mean radius and number density for Al12Mn, Al6Mn, Al45V7 and Al3Zr_D023 precipitates are compared against a long time (10^{12} s). Al45V7 missing in the modified database as it is not formed as per. The heat treatment conducted on the actual sample (1054 h) is illustrated with dotted lines.

molar volume of precipitates was entered based on calculations from the crystallographic information used for EBSD analysis [26]. A simplified growth model with spherical precipitates was assumed for all the precipitates. A mobility pre-factor of 10 was applied to better mimic the conditions existing in PBF-LB materials containing higher amounts of vacancies, like a quenched-like state of materials. The grain size of Al with radius = 10 μm and aspect ratio = 2 was assumed based on [15]. An isothermal calculation at 350 °C for 10^{12} s ($2.78*10^8$ h) was conducted to represent equilibrium-like conditions, similar to the experimental sample. It is to be noted that precipitation follows Becker's model [33] which is valid for coherent precipitation. The interfacial energy parameters were automatically selected from TC-PRISMA. The default values for Al12Mn, Al6Mn, Al3Zr_D023 and Al45V7 were 0.024 J/m^2, 0.047 J/m^2, 0.085 J/m^2 and 0.04 J/m^2 respectively. Precipitation of all possible phases as per Figs. 1 and 5 was done and it was assumed that precipitation takes place in bulk of the sample. The simulation was performed using the original set of thermodynamic parameters (Fig. 7a)) and using the modified database (Fig. 7b)). The kinetic parameters are the same for both simulations calculated using the MOBAL6 mobility database from Thermo-Calc Software AB. There is a clear decrease in the growth rates of precipitates when using the modified database. The mean radius of the Al12Mn precipitates has decreased from 42 nm → 5 nm and that of the Al6Mn precipitates has decreased from 21 nm → 4 nm for the performed simulation at 1054 h. This shows that the growth and coarsening of the Al6Mn and Al12Mn phases are significantly slowed down by the up-take of Cr in these Mn-rich precipitates. Additionally, selective precipitation at grain boundaries was observed as shown in Fig. 2, which could be explained by faster diffusion along grain boundaries giving rise to much faster growth rates locally [13,34,35]. Such a complex phenomenon cannot be captured easily using TC-PRISMA calculations for the time being. Finally, interfacial energies for the precipitates are valid for coherent precipitates only. Advanced characterization may be needed to calculate the interfacial energies to better capture the precipitation evolution. In summary, as compared to the sizes of precipitates in Figs. 2 and 3, the values obtained utilising TC-PRISMA are thus one to two orders of magnitude smaller from the size of precipitates observed for the bulk and two-three orders of magnitude from the grain boundary precipitates. We think that the current calculations are nonetheless valid for showing the general trend and to understand the effect of Cr in the Al–Mn–Cr–Zr alloys [13].

Cr addition is clearly shown to stabilise Mn-rich phases [21] thus providing higher strength via Orowan looping [36]. Fig. 8 schematically shows this strengthening increase. The Al–Zr precipitates primarily strengthen the matrix via shear hardening wherein strength increase is proportional to the mean radius at a given precipitate volume fraction. The Mn-rich precipitates harden the matrix via Orowan looping, wherein strength increase is inversely proportional to radius [36–38]. Although Orowan looping is a relatively poorer mechanism for strengthening, the amount of Mn-rich precipitates possible (up to 20–30 vol%) ought to contribute to the strengthening as both strengthening mechanisms are directly proportional to the volume fraction of precipitates formed. In the case (case 1) when Cr is not present in the alloys, there is a higher growth rate of Al12Mn precipitates. This means that peak hardening is obtained at shorter times. The peak strength (σ_p) at

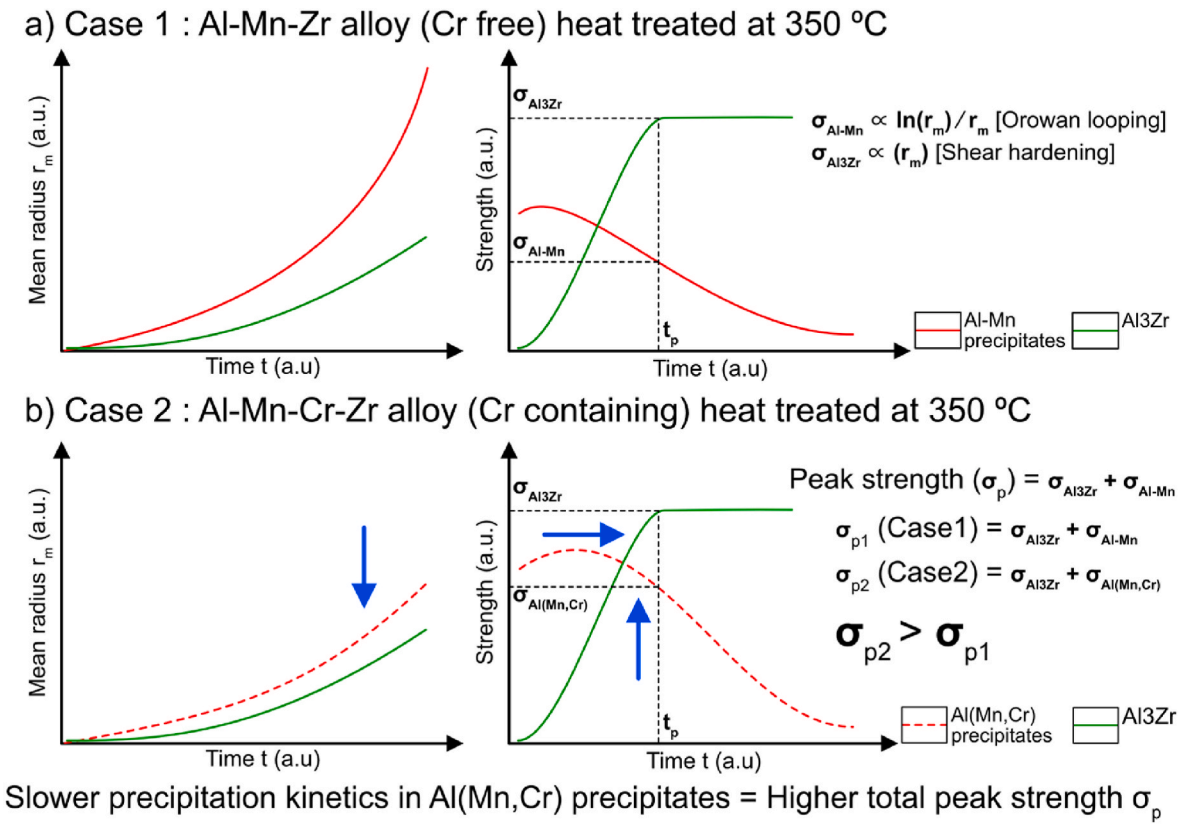

Fig. 8. Schematics of strength contribution in a) Case 1 (Al–Mn–Zr) alloy (Cr free) and b) Case 2 (Al–Mn–Cr–Zr) alloy (Cr containing). The curves on the left show the mean radius of precipitates (r_m) against time (t) and the curves on the right show the strength contribution from precipitates against time (t). All the axes are in arbitrary units (a.u.). The peak strength for the alloy in total (σ_p) is the combined contribution from strength from Al–Mn precipitates and Al3Zr precipitates.

optimised time (t_p) for such alloys would thus be lower. In case 2 when Cr is present, the slower growth kinetics of Al12Mn contribute to higher strength. This effect, combined with the contribution from Al–Zr precipitates produces the best hardening response in alloys containing Cr. There could be other microstructural observations to be considered such as co-precipitation of Al–Zr precipitates with Al–Mn precipitates (suggested before in Ref. [13]), possible strengthening from other precipitates such as AlMnSi_alpha or Al45Cr7 [39,40]. This might also affect the solubility of Mn, Cr in the Al-matrix which could thereby affect the precipitation kinetics of Al6Mn and Al12Mn. The exact precipitation mechanisms in these novel materials have not previously studied, and information from conventionally produced material is not directly applicable since the PBF-LB process creates materials with high supersaturation but severely distorted microstructures. A higher supersaturation of solutes makes it possible to create homogenous, controlled precipitation of coherent or semi-coherent precipitates that produce high strength. However, a severely deformed structure also increases vacancy or defect concentrations in places such as cell/dendrite boundaries or grain boundaries. This creates preferential sites for precipitation and affects diffusion, thus impacting the precipitation kinetics. To better understand this phenomenon, we conducted in-situ experiments for the same alloy [41] (*I.Lazar* et al., *under review*) at synchrotron facilities utilising the X-ray fluorescence technique. We could indeed see Cr and Mn segregating together when heat-treating thin foils in a controlled manner at 375 °C. The co-precipitation of Cr-rich precipitates with Mn-rich precipitates was observed, which was surprising. However, Cr enrichment did not lead to Mn depletion or vice versa hence still suggesting possible solubility of the elements in both precipitates during the initial part of heat treatment. Overall, this highlights the complexity of this precipitation phenomenon happening at the nanometric scale, which needs to be investigated further.

For the time being, the addition of thermodynamic parameters to available CALPHAD databases is a crucial step in understanding the novel alloys being created with the help of additive manufacturing. The schematics provided in Fig. 8 provides a way forward on how to optimise novel alloys produced by PBF-LB process. It shows that the addition of a ternary element into the hardening precipitate can slow down the kinetics and such a phenomenon can also be illustrated using CALPHAD methods. Such methods can later be used as an input for future alloy designs or heat treatments to get the best mechanical response from such alloys.

4. Conclusions

This study summarises the role of Cr in a novel Al–Mn–Cr–Zr-based family of alloys tailored for the additive manufacturing process called powder bed fusion-laser beam. Cr helps enhance the hardening contribution of Mn-rich precipitates and improves the high-temperature stability. In this study, the thermodynamic parameters for Cr containing Al–Mn precipitates from previous studies and optimised parameters were used for simulating the precipitation kinetics in TC-PRISMA. Overaged samples representing an equilibrium-like state were characterized to be used as a comparison for the study. Utilising these precipitation simulations with a modified database, a clearer understanding of the precipitation phenomenon could hence be developed. This helps develop optimised heat treatments for the Al–Mn–Cr–Zr alloys and acts as a guiding input for future alloy designs.

CRediT authorship contribution statement

B. Mehta: Writing – original draft, Validation, Software, Project administration, Methodology, Investigation, Funding acquisition,

Formal analysis, Data curation, Conceptualization. **K. Frisk:** Writing – review & editing, Validation, Supervision, Methodology, Funding acquisition, Data curation, Conceptualization. **L. Nyborg:** Writing – review & editing, Supervision, Funding acquisition, Conceptualization.

Declaration of competing interest

The authors declare that they have no known competing financial interests or personal relationships that could have appeared to influence the work reported in this paper.

Data availability

Data will be made available on request.

Acknowledgements

The authors would like to acknowledge the foundation for applied thermodynamics (Stiftelsen för Tillämpad Termodynamik) for funding this work between 2022 and 2023. Centre of Additive Manufacturing-Metal (CAM2) hosted by Chalmers University of Technology which is sponsored via VINNOVA grant number 2016–05175 is also acknowledged. The authors are thankful to Dr. Andreas Markström and Dr. Reza Naraghi from Thermo-Calc Software AB, Sweden for discussions to improve the work and provide correct software and databases.

Appendix A. Supplementary data

Supplementary data to this article can be found online at https://doi.org/10.1016/j.calphad.2024.102667.

Appendix

Atomic weights were taken from [42].

References

[1] T. DebRoy, H.L. Wei, J.S. Zuback, T. Mukherjee, J.W. Elmer, J.O. Milewski, A. M. Beese, A. Wilson-Heid, A. De, W. Zhang, Additive manufacturing of metallic components – process, structure and properties, Prog. Mater. Sci. 92 (2018) 112–224, https://doi.org/10.1016/j.pmatsci.2017.10.001.
[2] C. Emmelmann, P. Sander, J. Kranz, E. Wycisk, Laser additive manufacturing and bionics: redefining lightweight design, in: Phys Procedia, Elsevier B.V., 2011, pp. 364–368, https://doi.org/10.1016/j.phpro.2011.03.046.
[3] B. Blakey-Milner, P. Gradl, G. Snedden, M. Brooks, J. Pitot, E. Lopez, M. Leary, F. Berto, A. du Plessis, Metal additive manufacturing in aerospace: a review, Mater. Des. 209 (2021) 110008, https://doi.org/10.1016/j.matdes.2021.110008.
[4] W.E. Frazier, Metal additive manufacturing: a review, J. Mater. Eng. Perform. 23 (2014) 1917–1928, https://doi.org/10.1007/s11665-014-0958-z.
[5] H.H. König, N.H. Pettersson, A. Durga, S. Van Petegem, D. Grolimund, A. C. Chuang, Q. Guo, L. Chen, C. Oikonomou, F. Zhang, G. Lindwall, Solidification modes during additive manufacturing of steel revealed by high-speed X-ray diffraction, Acta Mater. 246 (2023), https://doi.org/10.1016/j.actamat.2023.118713.
[6] S. Thapliyal, M. Komarasamy, S. Shukla, L. Zhou, H. Hyer, S. Park, Y. Sohn, R. S. Mishra, An integrated computational materials engineering-anchored closed-loop method for design of aluminum alloys for additive manufacturing, Materialia (Oxf) 9 (2020) 100574, https://doi.org/10.1016/j.mtla.2019.100574.
[7] B. Mehta, L. Nyborg, K. Frisk, E. Hryha, Al–Mn–Cr–Zr-based alloys tailored for powder bed fusion-laser beam process: alloy design, printability, resulting microstructure and alloy properties, J. Mater. Res. 3 (2022) 1–13, https://doi.org/10.1557/s43578-022-00533-1.
[8] K. Schmidtke, F. Palm, A. Hawkins, C. Emmelmann, Process and mechanical properties: applicability of a scandium modified Al-alloy for laser additive manufacturing, Phys. Procedia 12 (2011) 369–374, https://doi.org/10.1016/j.phpro.2011.03.047.
[9] A. Plotkowski, K. Sisco, S. Bahl, A. Shyam, Y. Yang, L. Allard, P. Nandwana, A. M. Rossy, R.R. Dehoff, Microstructure and properties of a high temperature Al–Ce–Mn alloy produced by additive manufacturing, Acta Mater. 196 (2020) 595–608, https://doi.org/10.1016/j.actamat.2020.07.014.
[10] A.J. Ardell, Precipitation hardening, Metall. Trans. A 16 (1985) 2131–2165, https://doi.org/10.1007/BF02670416.
[11] ASM International, Introduction to aluminum and aluminum alloys, Metals Handbook Desk Edition (1998) 417–423, https://doi.org/10.31399/asm.hb.mhde2.a0003121.
[12] K.E. Easterling, D.A. Porter, Phase Transformations in Metals and Alloys, Second, Chapman & Hill, London, 1992.
[13] B. Mehta, K. Frisk, L. Nyborg, Effect of precipitation kinetics on microstructure and properties of novel Al-Mn-Cr-Zr based alloys developed for powder bed fusion – laser beam process, J. Alloys Compd. (2022), https://doi.org/10.1016/j.jallcom.2022.165870.
[14] A.B. Thermo-Calc Software, Precipitation Module (TC-PRISMA) User Guide, 2022, pp. 1–182. https://thermocalc.com/wp-content/uploads/Documentation/Archive/2020-2024/2022a/2022a-precipitation-module-tc-prisma-user-guide.pdf.
[15] B. Mehta, K. Frisk, L. Nyborg, S. Bengtsson, E. Hryha, Thermal Stability in Al-Mn-Cr-Zr Based Aluminium Alloys Tailored for Powder Bed Fusion – Laser Beam, WorldPM 2022 Congress & Exhibition : Conference Proceedings, 2022.
[16] J.O. Andersson, T. Helander, L. Höglund, P. Shi, B. Sundman, Thermo-Calc & DICTRA, computational tools for materials science, Calphad 26 (2002) 273–312, https://doi.org/10.1016/S0364-5916(02)00037-8.
[17] I. Ansara, A.T. Dinsdale, M.H. Rand, Thermochemical Database for Light Metal Alloys, 1998.
[18] B. Grushko, W. Kowalski, D. Pavlyuchkov, S. Balanetskyy, M. Surowiec, On the constitution of the Al-rich part of the Al-Cr-Mn system, J. Alloys Compd. 468 (2009) 87–95, https://doi.org/10.1016/j.jallcom.2007.12.069.
[19] S. Cui, I.H. Jung, Thermodynamic modeling of the Al-Cr-Mn ternary system, Metall Mater Trans A Phys Metall Mater Sci 48 (2017) 1383–1401, https://doi.org/10.1007/s11661-016-3894-8.
[20] L.F. Mondolfo, Al–Cr–Mn aluminum–chromium–manganese system, Aluminum Alloys 12 (1976) 483–485, https://doi.org/10.1016/b978-0-408-70932-3.50188-1.
[21] P. Liu, G.L. Dunlop, L. Arnberg, Microstructural development in a rapidly solidified Al5Mn2.5Cr alloy, Mater. Sci. Eng. 98 (1988) 437–441, https://doi.org/10.1016/0025-5416(88)90202-9.
[22] J. Adam, J.B. Rich, The crystal structure of WAl 12 , MoAl 12 and (Mn, Cr)Al 12, Acta Crystallogr. 7 (1954) 813–816, https://doi.org/10.1107/s0365110x54002514.
[23] A.D.I. Nicol, The structure of MnAl 6, Acta Crystallogr. 6 (1953) 285–293, https://doi.org/10.1107/s0365110x53000788.
[24] L.F. Mondolfo, Al–Fe–Mn aluminum–iron–manganese system, Aluminum Alloys (1976) 529–530, https://doi.org/10.1016/b978-0-408-70932-3.50229-1.
[25] A. Leicht, Laser Powder Bed Fusion of 316L Stainless Steel Microstructure and Mechanical Properties as a Function of Process, 2020.
[26] G. Bergerhoff, I.D. Brown, F. Allen, Crystallographic databases, International Union of Crystallography 360 (1987) 77–95.
[27] J.G. Barlock, L.F. Mondolfo, Structure of Some Aluminium-Iron-Magnesium-Manganese- Silicon Alloys, 1975, p. 66.
[28] E. Liotti, C.A. Kirk, I. Todd, K.S. Knight, S.C. Hogg, Synchrotron X-ray and neutron investigation of the structure and thermal expansion of the monoclinic Al13Cr2 phase, J. Alloys Compd. 781 (2019) 1198–1208, https://doi.org/10.1016/j.jallcom.2018.12.132.
[29] Y. Du, J. Wang, J. Zhao, J.C. Schuster, F. Weitzer, R. Schmid-Fetzer, M. Ohno, H. Xu, Z.K. Liu, S. Shang, W. Zhang, Reassessment of the Al-Mn system and a thermodynamic description of the Al-Mg-Mn system, Zeitschrift Fuer Metallkunde/Materials Research and Advanced Techniques 98 (2007) 855–871, https://doi.org/10.3139/146.101547.
[30] W.T. Elam, B.D. Ravel, J.R. Sieber, A new atomic database for X-ray spectroscopic calculations, Radiat. Phys. Chem. 63 (2002) 121–128, https://doi.org/10.1016/S0969-806X(01)00227-4.
[31] T. Ohnishi, Y. Nakatani, K. Shimizu, Constitution in the Solid State of Aluminum Rich Alloys in the Al-Mn-Cr Ternary System, vol. 8, 1972, https://doi.org/10.2464/jilm.22.8_504.
[32] J.W.H. Clare, Trans. Am. Inst. Min., Metall, Pet. Eng. 215 (1959) 429–433.
[33] R. Becker, Die Keimbildung bei der Ausscheidung in metallischen Mischkristallen, Ann Phys 424 (1938) 128–140, https://doi.org/10.1002/andp.19384240115.
[34] Y. Du, Y.A. Chang, B. Huang, W. Gong, Z. Jin, H. Xu, Z. Yuan, Y. Liu, Y. He, F. Y. Xie, Diffusion Coefficients of Some Solutes in Fcc and Liquid Al: Critical Evaluation and Correlation, Materials Science and Engineering A, 2003, https://doi.org/10.1016/S0921-5093(03)00624-5.
[35] N. Moelans, A. Miroux, E. Anselmino, S. Van Der Zwaag, B. Blanpain, P. Wollants, Phase-field simulations of coarsening of Al6Mn precipitates located on grain boundaries in AL alloys, TMS Annual Meeting (2009) 303–310.
[36] G.E. Dieter, Mechanical Metallurgy, McGraw-Hill Book Company, 1961.
[37] E. Nembach, Precipitation hardening caused by a difference in shear modulus between particle and matrix, Phys. Status Solidi 78 (1983) 571–581, https://doi.org/10.1002/pssa.2210780223.
[38] B. Mehta, High Performance Aluminium Alloys for Laser Powder Bed Fusion: Alloy Design and Development, 2021, p. 48. https://www.chalmers.se/sv/institutioner/ims/kalendarium/Sidor/High-Performance-Aluminium-Alloys-for-Laser-Powder.aspx%0A.
[39] Y.J. Li, A.M.F. Muggerud, A. Olsen, T. Furu, Precipitation of partially coherent α-Al(Mn,Fe)Si dispersoids and their strengthening effect in AA 3003 alloy, Acta Mater. 60 (2012) 1004–1014, https://doi.org/10.1016/j.actamat.2011.11.003.
[40] H.R. Leonard, S. Rommel, M.X. Li, S. Vijayan, T.J. Watson, T. Policandriotes, M. Aindow, Precipitation phenomena in a powder-processed quasicrystal-

reinforced Al-Cr-Mn-Co-Zr alloy, Mater. Char. 178 (2021), https://doi.org/10.1016/j.matchar.2021.111239.
[41] I. Lazar, B. Mehta, V. Bertschová, S.B.A. Malladi, Z. Ren, S. Das, J. Hagemann, G. Falkenberg, K. Frisk, A. Mikkelsen, L. Nyborg, In Situ Imaging of Precipitate Formation in Additively Manufactured Al-Alloys by Scanning X-Ray Fluorescence, 2023, https://doi.org/10.48550/arXiv.2311.14529.
[42] ACS Periodic Table of Elements, American Chemical Society (n.d.). https://www.acs.org/content/dam/acsorg/education/whatischemistry/periodic-table-of-elements/acs-periodic-table-poster_download.pdf (accessed March 22, 2023).